

Experimental Identification of the Dynamic Piezoresistivity of Fused-Filament-Fabricated Structures

Matic Arh, Janko Slavič, Miha Boltežar

^a*University of Ljubljana, Faculty of Mechanical Engineering, Aškerčeva 6, 1000 Ljubljana, Slovenia*

Cite as:

Matic Arh, Janko Slavič, and Miha Boltežar, Experimental identification of the dynamic piezoresistivity of fused-filament-fabricated structures, Additive Manufacturing, Volume 36, December 2020, <https://doi.org/10.1016/j.addma.2020.101493>

Abstract

Fused-filament-fabrication (FFF) technology is promising for the production of fully embedded piezoresistive dynamic sensors. However, the lack of experimental identification of the dynamic piezoresistivity limits the scientific and applied progress. Dynamic piezoresistivity of 3D printed structures is hard to research due to: structural anisotropy and heterogeneity, the large number of process parameters in 3D printing, the nonhomogeneous electric/stress/strain fields. Additionally, the piezoresistivity can be dependent on the frequency of the mechanical load and also on the temperature. This research proposes an experimental method to identify the dynamic piezoresistivity of unidirectionally printed specimens. The method is based on the Bridgman model of piezoresistivity and is extended to the dynamic conditions. With a single measurement, the stress in the specimen, the initial resistivity and the piezoresistive coefficient in the frequency domain are identified. The applicability of the method is experimentally tested on three specimens with different orientations of the mechanical and electrical loads. The identified piezoresistive coefficients identified using the proposed method can be used in analytical and numerical models in embedded, FFF dynamic sensors and similar applications.

Keywords: dynamic piezoresistivity, fused filament fabrication, piezoresistive coefficient, electric resistivity, frequency domain method, additive manufacturing

Email address: janko.slavic@fs.uni-lj.si (Janko Slavič)

1. Introduction

In recent years the production of smart materials suitable for additive manufacturing technologies has enabled the simultaneous production of multifunctional devices [1] *e.g.*, actuators [2, 3], embedded electric circuits [4, 5] and sensors [6, 7]. In the case of fused-filament-fabrication (FFF) technology, piezoresistive materials can be used to create sensors. Piezoresistivity denotes the phenomenon, whereby the electrical resistivity changes under the influence of mechanical strain [8].

In 2012 Leigh *et al.* developed a conductive thermoplastic material called “carbomorph” and showed that it is possible to use it with a 3D printer to print parts able to sense strain [9]. Recent years have seen a significant increase in the number of 3D printed sensors, *e.g.*, Alsharari *et al.* [10] researched graphene-based polylactic acid (PLA) and thermoplastic polyurethane (TPU) composite-based sensors, Christ *et al.* [11] researched TPU/multiwalled carbon nanotube (TPU/MWCNT) composite-based sensors, Gooding *et al.* [12] researched embedded tensile-strain sensors, Kim *et al.* researched a multiaxial force sensor [13], and Al-Rubaia *et al.* researched a strain sensor for sensing wind [14].

In 2019 Maurizi *et al.* researched dynamic strain measurements of FFF structures [15] and showed that it might be possible in the future to use FFF technology to produce reliable dynamic sensors. However, the manufacturing of reliable dynamic sensors is currently limited, since the influence on the dynamic piezoresistivity of FFF structures with applied loads in different directions is not well researched.

The FFF structure has to be electrically conductive in order to exhibit piezoresistive properties. Most of the materials used in the FFF process are, however, thermoplastics, which are electrically non-conductive. Conductivity is achieved by dispersing conductive particles in a non-conductive matrix: the conductivity of polymer composites is highly dependent on the volume ratio of the conductive particles, which is explained by the percolation theory [16]. Other mechanisms affecting the conductivity are tunneling and temperature effects [17]. In recent years the volume ratio of conductive parts was often researched, *e.g.*, composites of ABS/carbon nanotubes (CNT) [18], ABS/MWCNT [19], nylon 6/metal and high-density polyethylene [20], polypropylene/carbon black [21] and TPU/MWCNT [11]. Also investigated were the influences of the FFF process parameters on the electrical resistivity, *e.g.*, Tan *et al.* [20] researched the influence of the printing

orientation, Hampel *et al.* [22] the layer height, nozzle temperature and printing velocity, Zhang *et al.* [23] the layer thickness, raster width, and air-gap, and Watschke *et al.* researched the orientation, velocity and material flow [24]. In these studies a lower resistivity along the direction of the deposited material was achieved in comparison to the transverse direction. Furthermore, a 30-times-higher resistivity can be identified when poor electrical contacts are applied to the specimen [24]. The applicability of FFF as manufacturing technology for electric circuits and components was studied by Flowers *et al.* [25].

On the other hand, piezoresistivity as a material property has rarely been studied directly. While the piezoresistive behaviour of inkjet-printed thin films [26] and isotropic nanocomposites [27] has already been examined in terms of the tensor-based resistivity-strain relationship, the evaluation of the piezoresistivity of the FFF structures was limited to the resistance-change observations and gauge factors. For static and quasistatic FFF sensors, the influence of the geometry of the sensing part was researched by Gooding *et al.* [12], while Christ *et al.* [11] examined the influence of the content of conductive particles in a non-conductive polymer and Dawoud *et al.* [28] investigated the influence of raster gap and raster orientation on the static piezoresistivity. Dawoud *et al.* applied a static tensile load to a specimen and used a two-probe resistance measurement with different configuration electrodes; depending on the configuration of the electrodes, different piezoresistive properties were obtained, which indicates that electric boundary effects have an important impact on the piezoresistivity.

An important factor relating to the absence of dynamic piezoresistivity research is the lack of methods for dynamic piezoresistivity identification. Several difficulties arise when the piezoresistivity of FFF structures is identified *e.g.*, the anisotropy, the heterogeneity, the large number of 3D printing process parameters, the difficulty with electrical contacts, the dependency of the load frequency and finally the temperature dependence. Due to the anisotropy and heterogeneity it is difficult to simultaneously establish a homogenous electric and stress/strain field. To overcome the existing issues, a new method is proposed, based on unidirectionally printed specimens that can be used to estimate the dynamic piezoresistivity of FFF structures with the mechanical load and electrical field established in the same direction. Since many of the design principles of piezoresistive dynamic sensors are based on the electric field and stress being parallel [8], the obtained coefficients are widely applicable. Coefficients can be used in numerical and analytical models and to estimate the effects of process parameters.

This manuscript is organized as follows: Sec. 2 gives the theoretical

background on the theory of elasticity and electric conductivity, Sec. 3 introduces the method for dynamic piezoresistivity identification, Sec. 4 gives the background on the experimental research, Sec. 5 presents the experimental results and, finally, Sec. 7 gives the conclusions.

2. Theoretical background

The large variety of possible raster patterns results in the local microstructural behaviour of FFF structures. However, effective homogenised properties can be used to predict their macroscopical behaviour [29, 30], especially when the infill density is close to 100%. Ohm's law for a homogeneous anisotropic structure relates the electric field intensity \mathbf{E} and the electric current density \mathbf{J} through the resistivity matrix $\boldsymbol{\rho}$ as [31]:

$$\begin{Bmatrix} E_1 \\ E_2 \\ E_3 \end{Bmatrix} = \begin{bmatrix} \rho_{11} & \rho_{12} & \rho_{13} \\ \rho_{21} & \rho_{22} & \rho_{23} \\ \rho_{31} & \rho_{32} & \rho_{33} \end{bmatrix} \begin{Bmatrix} J_1 \\ J_2 \\ J_3 \end{Bmatrix} \quad (1)$$

or using the summation convention:

$$E_i = \rho_{ij} J_j, \quad i, j = 1, 2, 3 \quad (2)$$

where the indices i, j represent the orthogonal basis vector directions \mathbf{e}_1 , \mathbf{e}_2 and \mathbf{e}_3 . The piezoresistive behaviour is described using the Bridgman piezoresistivity model [32]:

$$\rho_{ij} = \rho_{0ij} + d\rho_{ij} = \rho_{0ij} \left(1 + \frac{d\rho_{ij}}{\rho_{0ij}} \right), \quad i, j = 1, 2, 3. \quad (3)$$

where ρ_{0ij} represents the initial resistivity when no mechanical load is applied to the specimen and $d\rho_{ij}$ is the increment of the resistivity due to the mechanical load. In general, the initial resistivity ρ_{0ij} is temperature dependent. However, in this research a constant temperature is assumed. The relative resistivity change $d\rho_{ij}/\rho_{0ij}$ linearly depends on the strain ε_{kl} as [33]:

$$d\rho_{ij}/\rho_{0ij} = \xi_{ijkl} \varepsilon_{kl}, \quad i, j, k, l = 1, 2, 3 \quad (4)$$

where ξ_{ijkl} represents the piezoresistive coefficient. Using Voigt-Kelvin notation, which simplifies the two-subscript notation into a single-subscript

notation [34]:

$$11 \rightarrow 1, \quad 22 \rightarrow 2, \quad 33 \rightarrow 3, \quad 23 \rightarrow 4, \quad 13 \rightarrow 5, \quad 12 \rightarrow 6 \quad (5)$$

Eq. (4) simplifies to

$$d\rho_i/\rho_{0i} = \xi_{ij} \varepsilon_j, \quad i, j = 1, \dots, 6. \quad (6)$$

Under the assumption of a linear elasticity hypothesis, the strain and stress σ_j relationship is equal to [34]:

$$\varepsilon_i = s_{ij} \sigma_j, \quad i, j = 1, \dots, 6 \quad (7)$$

where s_{ij} denotes the compliance coefficients. As a result, the relative resistivity change can be written in terms of the stress:

$$d\rho_i/\rho_{0i} = \xi_{ij} s_{jk} \sigma_k = \pi_{ik} \sigma_k, \quad i, j, k = 1, \dots, 6 \quad (8)$$

where π_{ik} represents the piezoresistive coefficient relating the relative resistivity change $d\rho_i/\rho_{0i}$ and the stress σ_k . When the structures are manufactured with material being deposited in a single direction, as shown in Fig. 1 a), the symmetry of the material properties in three orthogonal planes is assumed (along the deposited material, and transverse in the horizontal and vertical planes) [35, 36], resulting in orthotropic material properties:

$$\boldsymbol{\pi} = \begin{bmatrix} \pi_{11} & \pi_{12} & \pi_{13} & 0 & 0 & 0 \\ \pi_{21} & \pi_{22} & \pi_{23} & 0 & 0 & 0 \\ \pi_{31} & \pi_{32} & \pi_{33} & 0 & 0 & 0 \\ 0 & 0 & 0 & \pi_{44} & 0 & 0 \\ 0 & 0 & 0 & 0 & \pi_{55} & 0 \\ 0 & 0 & 0 & 0 & 0 & \pi_{66} \end{bmatrix}, \quad \boldsymbol{\rho} = \begin{bmatrix} \rho_1 & 0 & 0 \\ 0 & \rho_2 & 0 \\ 0 & 0 & \rho_3 \end{bmatrix}. \quad (9)$$

The article is focused on a special case, when the electric field intensity \mathbf{E} , the electric current density \mathbf{J} and the stress $\boldsymbol{\sigma}$ are in the directions of the material symmetry as shown in Figs. 1 b), c) and d). Ohm's law and the relative resistivity change for the case shown in Fig. 1 b) are:

$$E_1 = \rho_1 J_1, \quad (10)$$

$$\frac{d\rho_1}{\rho_{01}} = \pi_{11} \sigma_1. \quad (11)$$

Ohm's law and the relative resistivity change for the case shown in Fig. 1 c):

$$E_2 = \rho_2 J_2, \quad (12)$$

$$\frac{d\rho_2}{\rho_{02}} = \pi_{22} \sigma_2 \quad (13)$$

and for Fig. 1 d):

$$E_3 = \rho_3 J_3, \quad (14)$$

$$\frac{d\rho_3}{\rho_{03}} = \pi_{33} \sigma_3. \quad (15)$$

Equations (10) - (15) show that the piezoresistivity in material's principle directions π_{11} , π_{22} and π_{33} can be identified by establishing the stress and electric fields in the material's principle directions.

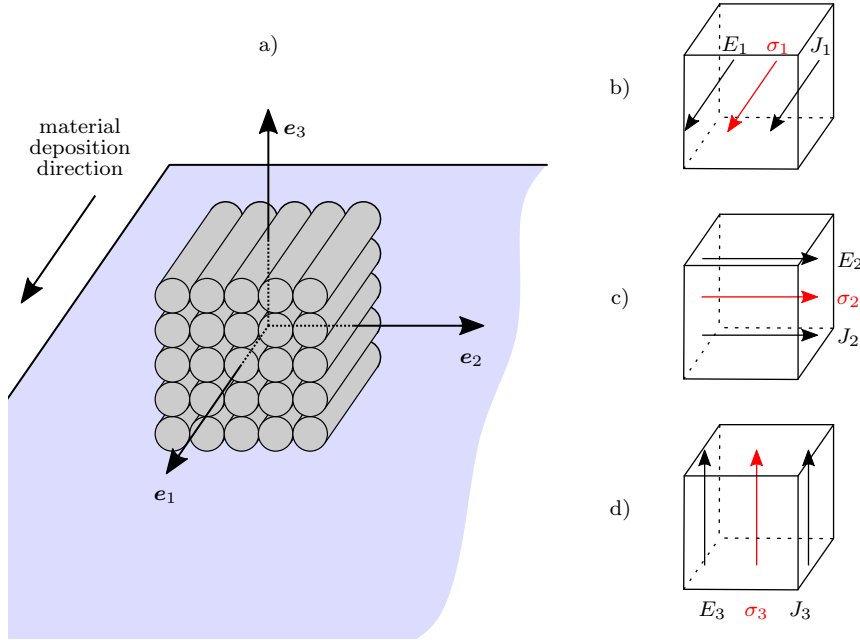


Figure 1: a) Unidirectional FFF structure; Homogenised equivalent with b) electric field intensity \mathbf{E} , current density \mathbf{J} and stress $\boldsymbol{\sigma}$ in the direction \mathbf{e}_1 , c) \mathbf{E} , \mathbf{J} , and $\boldsymbol{\sigma}$ in the direction \mathbf{e}_2 and d) \mathbf{E} , \mathbf{J} , and $\boldsymbol{\sigma}$ in the direction \mathbf{e}_3

3. Method

3.1. Specimens

The specimen orientation with regard to the load cases shown in Figs. 1 b), c) d) are shown in Fig. 2 as O1, O2 and O3, respectively. The dimensions of the specimens are $l_1 = 110$ mm, $l_2 = 20$ mm and $l_3 = 7$ mm. A harmonic mechanical excitation with no offset is applied to the specimens. Due to the compressive phase of the excitation, buckling should be prevented. The critical buckling load that should not be exceeded is approximately 290 N (for a Young's modulus of 2 GPa)

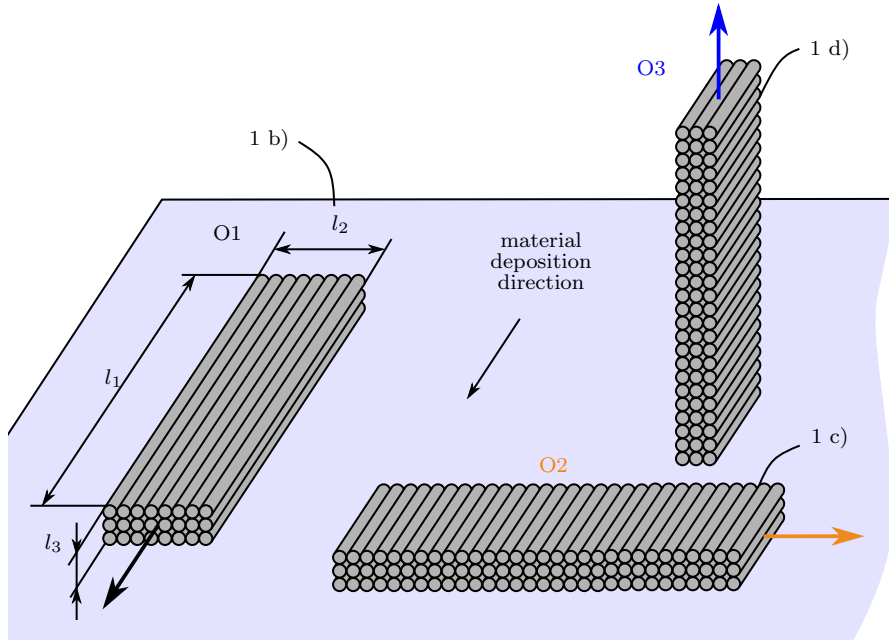


Figure 2: Specimen: arrows indicate mechanical load direction

3.2. Electrical contacts

The electrical contact preparation is shown in Fig. 3. In the first step, the surface of the electrically conductive specimen is coated with a silver paint [37] and left to dry. In the second step, a thin enamelled copper wire is soldered to the conductive copper tape [38], which is then taped to the specimen at the location of the silver paint. A relatively thin wire has to be used, to prevent any significant contribution to the specimen's dynamics.

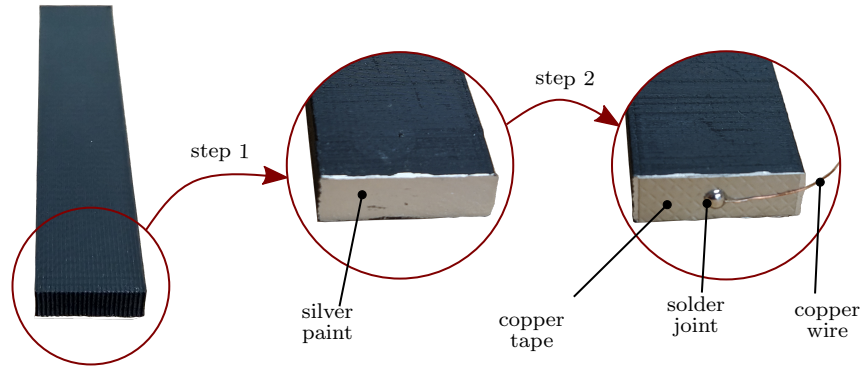


Figure 3: Preparation of electrical contacts

3.3. Piezoresistivity identification

Fig. 4 shows the proposed experimental setup for the identification of the piezoresistivity. The specimen is mechanically fixed on one side, while it is able to move in the axial direction on the other side. In this section, if not otherwise noted, the orientation of specimen O1 is assumed, see Fig. 2. Dimension $l_C = 30$ mm denotes the clamping length.

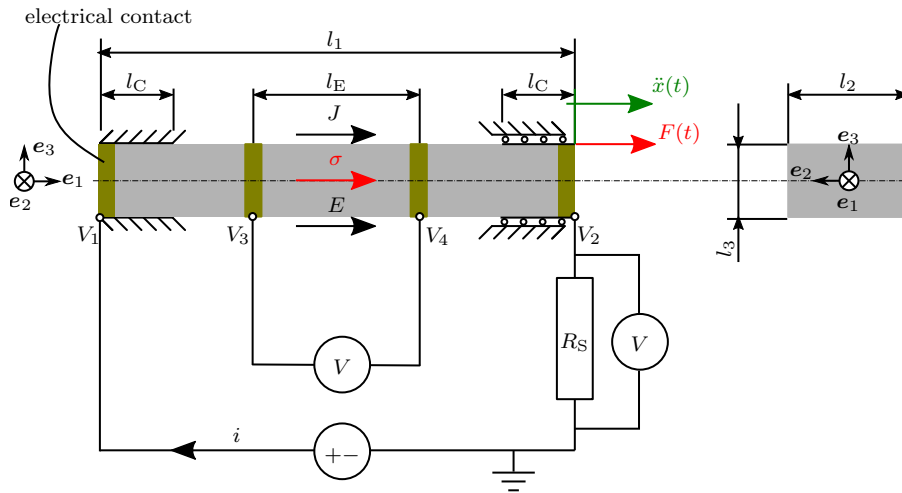


Figure 4: Schematic diagram of proposed experimental setup

For the identification of the electrical resistivity, the four-probe method [39] is used to measure the specimen's resistance. The electrical contacts have

the electric potentials V_1, V_2, V_3 and V_4 . The contacts V_3 and V_4 are $l_E = 10$ mm apart and are assumed to be in the electrical and mechanical homogeneous zone without boundary effects (*e.g.*, due to clamping, electrodes, for details see Appendix A). The supply circuit is connected to the contacts V_1 and V_2 , which are l_1 apart. The electrical current through the specimen i is determined through the voltage drop across the shunt resistor u_S with resistance R_S , see Fig. 4:

$$i = \frac{u_S}{R_S}. \quad (16)$$

By measuring the voltage drop between the contacts V_3 and V_4 , the electrical resistance of the 3D printed structure between the contacts is determined as:

$$R = \frac{V_3 - V_4}{i} = \frac{u_R}{i}. \quad (17)$$

Due to the geometrical relationship between the resistance R and the resistivity ρ_1 it follows that [40]:

$$\rho_1 = R \frac{(l_2 + dl_2)(l_3 + dl_3)}{l_E + dl_E} = \frac{u_R}{i} \frac{(l_2 + dl_2)(l_3 + dl_3)}{l_E + dl_E}, \quad (18)$$

where dl_2, dl_3, dl_E denote the length changes of l_2, l_3 and l_E due to the applied load, respectively. Under a uniaxial stress assumption, the strain equals:

$$\varepsilon_1 = \frac{dl_E}{l_E}, \quad \varepsilon_2 = \frac{dl_2}{l_2} = -\nu_{12} \varepsilon_1, \quad \varepsilon_3 = \frac{dl_3}{l_3} = -\nu_{13} \varepsilon_1, \quad (19)$$

and equation (18) simplifies to:

$$\rho_1 = R \frac{l_2 l_3}{l_E} \underbrace{\frac{(1 - \nu_{12} \varepsilon_1)(1 - \nu_{13} \varepsilon_1)}{1 + \varepsilon_1}}_{\text{geometrical changes}}, \quad (20)$$

where ν_{12} and ν_{13} denote the Poisson's ratio relating the axial strain ε_1 with the transverse strain ε_2 and ε_3 , respectively. The influence of the geometrical changes in Eq. (20) are discussed in Appendix B.

This research is focused on the harmonic changes in the resistivity when

a harmonic load $F(t)$ is applied to the moving end, see Fig. 4:

$$F(t) = \tilde{F} e^{i2\pi f_{\text{exc}} t}, \quad (21)$$

where \tilde{F} denotes the force amplitude, i is an imaginary number, π is the number Pi, f_{exc} is the excitation frequency in Hz and t is time. For a causal, linear system, the harmonic force causes a harmonic displacement $x_1(t)$, a stress $\sigma_1(t)$, strain $\varepsilon_1(t)$ and also a resistivity $\rho_1(t)$ in the axial direction. The strain in the axial direction $\varepsilon_1(t)$ is estimated from the displacement $x_1(t)$:

$$\varepsilon_1(t) = \frac{x_1(t)}{l_1 - 2l_C}, \quad (22)$$

and the Poisson's ratios ν_{12} and ν_{13} (20) can be estimated from a static tensile test or by simultaneous measurements of the transverse strain $\varepsilon_2(t)$ and $\varepsilon_3(t)$. The measured resistivity ρ_1 (3)(20):

$$\rho_1(t) = \rho_{01} + d\rho_1(t). \quad (23)$$

is related to the underlying resistivity coefficient via Eq. (11); however, due to the assumed constant temperature, ρ_{01} is related to the mean value $\rho_{01} = \text{Mean}(\rho_1)$ and the changes in resistivity $d\tilde{\rho}_1$ to the amplitude at the excitation frequency f_{exc} . The amplitude spectrum $\tilde{\rho}_1(f)$ is obtained by transforming the resistivity $\rho_1(t)$ into the frequency domain using a Fourier transform. The resistivity ρ_{01} and the resistivity change $d\tilde{\rho}_1$ are obtained as:

$$\rho_{01} = \tilde{\rho}_1(f = 0), \quad (24)$$

$$d\tilde{\rho}_1 = \tilde{\rho}_1(f = f_{\text{exc}}). \quad (25)$$

At the excitation frequency f_{exc} , due to the harmonic response, the piezoresistivity coefficient π_{11} (11) can be related to the amplitude of the change in resistivity $\tilde{\rho}_1(f_{\text{exc}})$, the amplitude in the mechanical stress $\tilde{\sigma}(f_{\text{exc}})$ and the initial resistivity $\tilde{\rho}_1(f = 0)$:

$$\pi_{11}(f_{\text{exc}}) = \frac{\tilde{\rho}_1(f_{\text{exc}})}{\tilde{\rho}_1(f = 0) \tilde{\sigma}(f_{\text{exc}})}. \quad (26)$$

The amplitude of the mechanical stress $\tilde{\sigma}(f_{\text{exc}})$ is defined as, see Fig 2:

$$\tilde{\sigma}(f_{\text{exc}}) = \frac{\tilde{F}_{\text{R}}(f_{\text{exc}})}{l_2 l_3}, \quad (27)$$

where $\tilde{F}_{\text{R}}(f_{\text{exc}})$ is the amplitude of the force in the specimen, which can be related to the measured force amplitude $\tilde{F}(f_{\text{exc}})$:

$$\tilde{F}_{\text{R}}(f_{\text{exc}}) = \tilde{F}(f_{\text{exc}}) - m \ddot{x}(f_{\text{exc}}), \quad (28)$$

where m is the moving mass and \ddot{x} is the measured acceleration amplitude of the moving mass. Further, the moving mass m is estimated as:

$$m = m_{\text{C}} + m_{\text{S}} \left(1 - \frac{l_{\text{C}}}{l_1}\right), \quad (29)$$

where $m_{\text{C}} = 0.403 \text{ kg}$ is the mass of the fixation clamps at one side and $m_{\text{S}} \approx 0.01 \text{ kg}$ is the mass of the specimen. As a reasonable approximation, in Eq. (29) the complete mass of the specimen except the clamped length l_{C} was assumed to be moving.

To summarize: based on the measured values $F(t)$, $\ddot{x}(t)$, $u_{\text{S}}(t)$, $u_{\text{R}}(t)$, the coefficient of piezoresistivity for the specimen orientation O1, *i.e.*, π_{11} Eq (26), can be identified. The specimen orientations O2 and O3 can be used for the identification of the piezoresistivity coefficients π_{22} and π_{33} , respectively. For the O2 and O3 orientations, the resistivity in Eq. (26) changes as follows:

$$\text{O2, } \pi_{22} : \quad \tilde{\rho}_1 \rightarrow \tilde{\rho}_2 \quad (30)$$

$$\text{O3, } \pi_{33} : \quad \tilde{\rho}_1 \rightarrow \tilde{\rho}_3 \quad (31)$$

4. Experiment

4.1. Specimen preparation

Specimens with the orientations O1, O2 and O3 (Fig. 2) were 3D printed with a PRUSA I3 MK3S. Two specimens for each orientation were manufactured, resulting in a total of 6 specimens. An electrically conductive composite filament from Proto-pasta [41] with a diameter of 1.75 mm was used. The conductive Proto-pasta filament consists of a non-conductive PLA matrix and conductive carbon-black particles. Based on the studies of Maurizi *et al.* [15] and Munasinge [42], a linear piezoresistive behaviour in $\varepsilon < 0.5 \%$ is assumed. The printing parameters were layer height 0.15 mm,

infill density 100%, printing temperature of the conductive PLA 225°C, built plate temperature 70°C, line width 0.4 mm, lines as infill pattern.

4.2. Experimental setup

The experimental setup is shown in Fig. 5. The specimen is clamped between one fixed clamp attached to the support structure and one clamp attached to a LDS V555 eletrodynamical shaker. In order to electrically insulate the specimen from the environment, a thin insulating tape at the interface between the specimen and clamping was used. The acceleration and force from Fig. 4 were measured with a PCB T333B30 accelerometer and a PCB 218C charge force sensor, which were mounted between the shaker and the moving clamp. With a force sensor the Brüel and Kjør Nexus 2692 charge pre-amplifier was used. The signal from the accelerometer and force sensor were acquired using a National Instruments 9234 measuring card.

A constant voltage was supplied to the specimen using a HQ-Power PS23023 adjustable DC power supply. The voltage drop across the current shunt and specimen, see Fig.4, were acquired using a National Instruments 9215 measuring card.

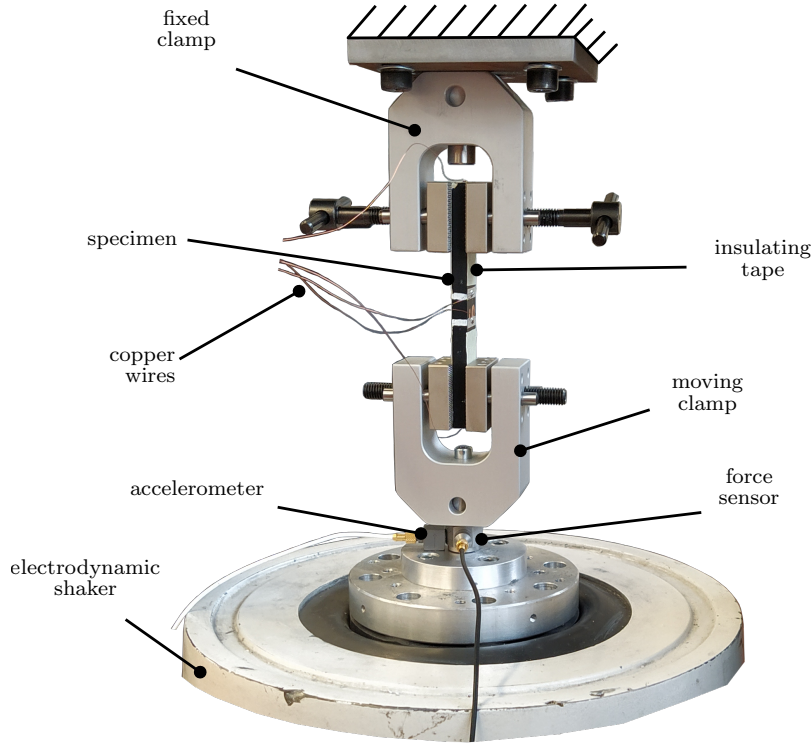


Figure 5: Experimental setup

4.3. Measurements

The specimen was supplied with a constant voltage and current of approximately 10 mA. The electrodynamic shaker excited the specimen with a displacement amplitude of $40 \mu\text{m}$ at selected frequencies (55 Hz, 110 Hz, 165 Hz and 220 Hz) for 30 s. The excitation frequencies were significantly below the first natural frequency of the system, which was identified in the range 500-550 Hz (depending on the specimen orientation). The displacement amplitude of $40 \mu\text{m}$ causes a normal strain of 0.08 %, which is assumed to be in the linear region. When linearity cannot be assumed, the piezoresistive coefficients at different displacement amplitudes have to be determined to find the linear region. The identification of the dynamic piezoresistivity (26) is based on the simultaneously measured force $F(t)$, acceleration $\ddot{x}(t)$, voltage drops $u_R(t)$ and $u_S(t)$. The voltage drops $u_R(t)$ and $u_S(t)$ were used to determine the resistivity $\rho(t)$ (20). Poisson's ratios $\nu_{12} = 0.37$ and $\nu_{13} = 0.38$ were determined for the O1 oriented specimen using a static tensile test. Poisson's ratio $\nu_{12} = \nu_{13} = \nu = 0.375$ was used

for the geometrical correction in Eq. (20).

The measured force $F(t)$, acceleration $\ddot{x}(t)$ and resistivity $\rho(t)$ were, using a Fourier transform, transformed from the time to the frequency domain. A particular 30-s-long time-domain signal was, due to averaging, divided into 30 non-overlapping segments of length 1 s (a Hanning window was used). Python library SciPy [43] was used for signal processing. The resulting amplitude complex spectra are $\tilde{F}(f)$, $\tilde{\ddot{x}}(f)$, $\tilde{\rho}(f)$, see, *e.g.*, Fig. 6 for the O3-oriented specimen at $f_{\text{exc}} = 220$ Hz excitation frequency. From the amplitude spectra, complex amplitudes at the excitation frequency $\tilde{F}(f_{\text{exc}})$, $\tilde{\ddot{x}}(f_{\text{exc}})$, $\tilde{\rho}(f_{\text{exc}})$ and static resistivity $\tilde{\rho}(f = 0)$ were obtained to identify the piezoresistive coefficient, see Fig. 6 and Eqs. (26), (27), (28).

5. Results

Time- and frequency-domain results for the specimen orientation O3 at 220 Hz harmonic excitation are shown in Fig. 6. The major findings from the results are:

- Static resistivity $\tilde{\rho}(f = 0) \approx 34.3$ Ohm cm is approximately three orders of magnitude higher than the harmonic resistivity at the excitation frequency $\tilde{\rho}(f_{\text{exc}})$ which is further approximately three orders of magnitude above the noise floor.
- Stress in the specimen $\tilde{\sigma}(f_{\text{exc}})$ is based on the amplitude of the excitation force $\tilde{F}(f_{\text{exc}})$ and acceleration $\tilde{\ddot{x}}(f_{\text{exc}})$. Force and acceleration amplitudes are approximately five and four orders of magnitude above the noise floor, respectively. Both are contaminated with electromagnetic noise (especially at 100 Hz).

Similar results were obtained for other specimen orientations and excitation frequencies.

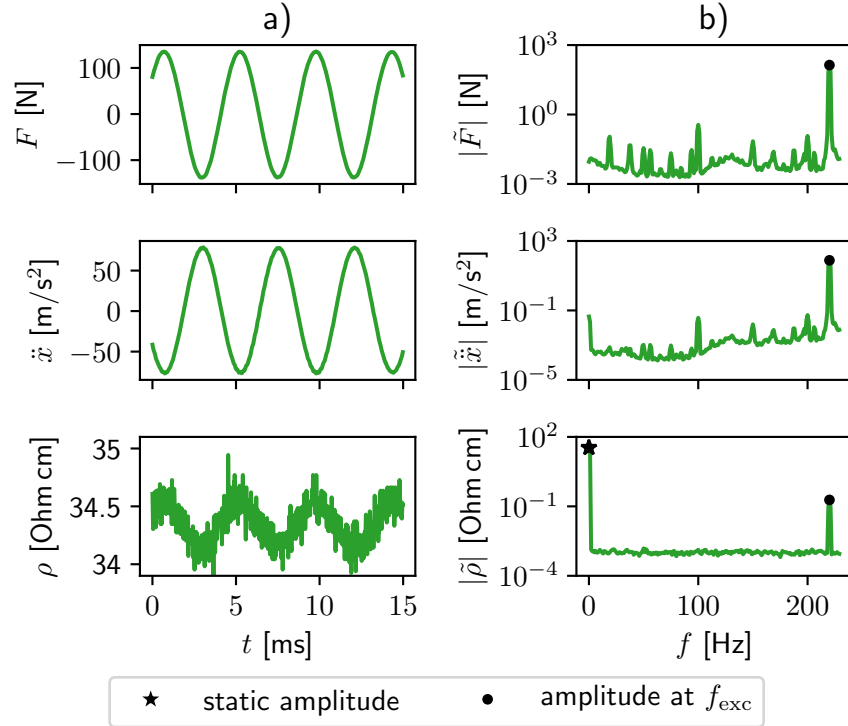


Figure 6: a) Measured time signals, b) complex amplitudes in frequency domain of specimen with orientation O3 at 220 Hz excitation frequency

In Tab. 1 the identified mean amplitudes at measured excitation frequencies (55 Hz, 110 Hz, 165 Hz, 220 Hz) and the piezoresistive coefficient for O1, O2, O3 specimen orientations are presented. The specimens exhibited a low viscoelastic behaviour (phase shift of less than 3°). Due to the low impact on the final result (less than 1%), absolute values with the appropriate sign (+/-) are used for calculations of the results in Tab 1, instead of complex amplitudes. Based on the results in Tab 1, the following observation were made:

- Initial resistivity $\rho_0 = \tilde{\rho}(0)$ does not depend on the frequency with $\rho_{01} = 20.96 \pm 1.21$ Ohm cm, $\rho_{02} = 32.96 \pm 0.62$ Ohm cm, $\rho_{03} = 33.83 \pm 1.08$ Ohm cm.
- Amplitude of acceleration is constant at a certain frequency point and negative, as the system is operating below the resonance frequency.
- Force $\tilde{F}(f_{\text{exc}})$ decrease with frequency.

- The highest piezoresistive coefficient is exhibited by orientation O3 $\pi_{33} = 3.54 \pm 0.11 \text{ GPa}^{-1}$, followed by O2 $\pi_{22} = 2.30 \pm 0.41 \text{ GPa}^{-1}$ and O1 $\pi_{11} = 0.17 \pm 0.05 \text{ GPa}^{-1}$.

Table 1: Identified average amplitudes used for calculation of the piezoresistive coefficient and identified piezoresistive coefficient for different specimen orientations and excitation frequencies

orientation	f [Hz]	specimen	$\tilde{\rho}(0)$ [Ohm cm]	$\tilde{\rho}(f_{exc})$ [Ohm mm]	$\tilde{F}(f_{exc})$ [N]	$\tilde{x}(f_{exc})$ [m s ²]	$\pi(f_{exc})$ [GPa ⁻¹]	
O1	55	1	21.54	0.04	172.06	-4.81	0.15	
		2	20.20	0.05	173.95	-4.81	0.21	
	110	1	21.61	0.03	163.00	-19.18	0.13	
		2	20.45	0.04	163.70	-19.28	0.16	
	165	1	21.60	0.04	159.05	-43.02	0.15	
		2	20.34	0.05	159.60	-43.31	0.19	
	220	1	21.50	0.04	143.37	-76.06	0.16	
		2	20.47	0.05	145.10	-76.86	0.18	
	O2	55	1	32.84	1.04	175.90	-4.81	2.49
			2	33.14	0.89	173.10	-4.81	2.15
110		1	32.43	1.02	164.21	-19.19	2.56	
		2	33.40	0.83	161.80	-19.28	2.04	
165		1	32.70	1.03	159.87	-43.01	2.48	
		2	33.31	0.88	156.90	-43.31	2.12	
220		1	32.76	1.02	144.12	-75.88	2.48	
		2	33.10	0.87	142.21	-76.86	2.10	
O3		55	1	34.35	1.46	163.32	-4.81	3.61
			2	33.05	1.40	165.01	-4.81	3.54
	110	1	34.13	1.41	152.50	-19.18	3.60	
		2	33.43	1.38	155.00	-19.26	3.55	
	165	1	34.19	1.46	148.72	-43.02	3.58	
		2	33.39	1.42	150.76	-43.30	3.53	
	220	1	34.67	1.42	134.66	-76.06	3.43	
		2	33.43	1.41	137.51	-76.85	3.48	

6. Discussion

Due to the lack of research, the piezoresistive coefficients π are hard to compare to previous experiments; however, the initial resistivity ρ_0 can be compared to previous research, see Tab. 2. The results are in reasonable agreement with the research of Watschke *et al.* [24] and Hampel *et al.* [22]. The resistivity in the deposition direction ρ_{01} in comparison with ρ_{02} and ρ_{03} is smaller due to the additional resistivity of the adjacent traces for ρ_{02} and ρ_{03} . Hampel *et al.* examined the increase of the resistivity due to the

adjacent traces and found that it is the same for horizontal and vertical (build-up) directions. This finding by Hampel *et al.* is similar to that reported here ($\rho_{02} \approx \rho_{03}$).

Table 2: Initial resistivity comparison

Initial resistivity [Ω cm]	This research, Tab. 1	Watschke et al. [24]	Hampel et al. [22]
ρ_{01}	≈ 20.96	$6 < \rho_1 < 16$	4.94
ρ_{02}	≈ 32.96	$11 < \rho_2 < 24$	/
ρ_{03}	≈ 33.83	/	/

While there is no significant difference of the initial resistivity in the directions ρ_{02} and ρ_{03} , the piezoresistive coefficients π_{22} and π_{33} differ significantly. This can be attributed to the different mechanical bonding strength of the adjacent traces. Since the FFF parts are built layer by layer a lower temperature field appears when the material is deposited in the vertical direction due to the cooling of already-deposited material. A lower temperature results in a lower bonding strength in the vertical direction, as compared to the horizontal plane, see [44], [45]. Weaker mechanical bonding could cause the conductive networks to break and form more easily, resulting in a higher piezoresistive coefficient π_{33} .

7. Conclusions

A method for the identification of the dynamic piezoresistive coefficients of unidirectional FFF structures was proposed. The method is based on the Bridgman model of piezoresistivity and is extended to harmonic mechanical excitation. Three build orientations of the specimens were used to identify the piezoresistive properties in three orthogonal directions. Based on the simultaneous measurement of force, acceleration and voltage drops across the specimen and the shunt resistor the dynamic piezoresistive coefficient can be identified.

The method was successfully implemented on three orthogonally manufactured specimens in the 55 Hz-220 Hz frequency range. Significantly different piezoresistive coefficients were identified: $\pi_{11} = 0.17 \pm 0.05 \text{ GPa}^{-1}$, $\pi_{22} = 2.30 \pm 0.41 \text{ GPa}^{-1}$ and $\pi_{33} = 3.54 \pm 0.11 \text{ GPa}^{-1}$ for the O1, O2 and O3 orientations, respectively. In the researched frequency range, the piezoresistive coefficients were found to be constant.

The identified piezoresistive coefficients in different directions enable the future numerical and analytical research on advance dynamic sensors with an arbitrary spatial orientation of embedding.

Acknowledgements

The authors acknowledge the partial financial support from the Slovenian Research Agency (research core funding No. P2-0263).

Appendix A. Effects of the finite length of the electrodes on the identified resistivity

Electrical contacts with voltages V_1 and V_2 (see Fig. 5) are applied to the l_2 - l_3 faces. As a result, a homogenous electric field can be assumed in the axial direction. In order to avoid the effects of clamping, the voltage drops between the electrodes V_3 and V_4 are measured to determine the resistivity in Sec. 3.3. However, the finite length of the electrodes V_3 , V_4 , can influence the measured resistivity. To check whether the electrodes V_3 and V_4 have a significant influence on the measurement, three resistivity measurements on the O1 oriented specimen were performed. Figure A.7 shows the preparation of the specimen. In the first step, only the contacts V_1 and V_2 were prepared, as described in 3.2 and shown in Fig. A.7 a). The resistivity ρ_{M1} was determined from the voltage drop between V_1 and V_2

$$\rho_{M1} = \frac{V_1 - V_2}{i} \frac{l_2 l_3}{l_1}. \quad (\text{A.1})$$

In the second step, the electrical contacts V_3 and V_4 were prepared, see Fig. A.7 b). The resistivity ρ_{M2} was determined from the voltage drop between V_1 and V_2 using Eq. (A.1). Lastly, the resistivity ρ_{M3} was determined from voltage drop between V_3 and V_4 as:

$$\rho_{M3} = \frac{V_3 - V_4}{i} \frac{l_2 l_3}{l_E}. \quad (\text{A.2})$$

The measured resistivities were $\rho_{M1} = 21.9$ Ohm cm, $\rho_{M2} = 21.8$ Ohm cm and $\rho_{M3} = 21.4$ Ohm cm. Based on the results, the impact of the electrodes is in the range of approximately 2% and was neglected in this study.

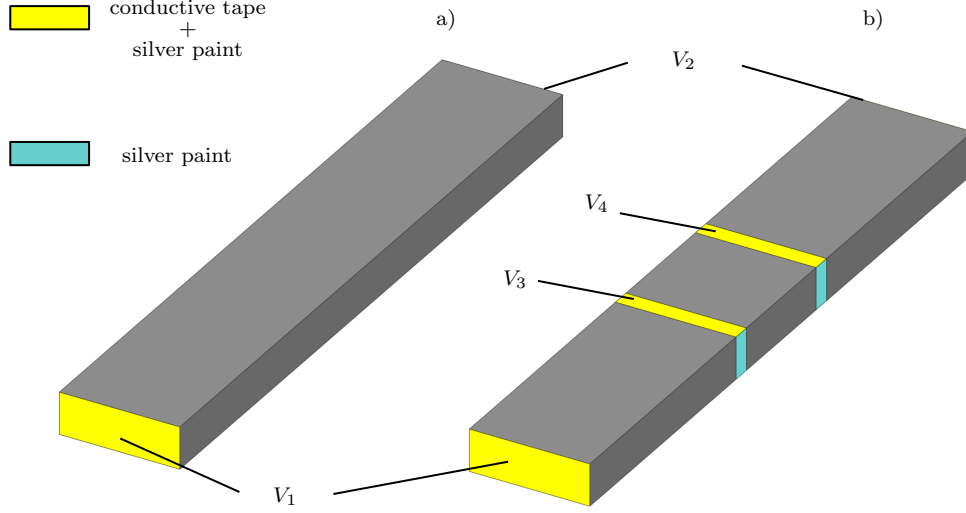


Figure A.7: Specimen preparation for determination: a) ρ_{M1} , b) ρ_{M2} and ρ_{M3}

Appendix B. The effects of the correction of geometrical changes on the identified piezoresistivity

In Eq. (20) the resistivity is determined by taking into account the geometrical changes:

$$g = \frac{(1 - \nu_{12} \epsilon_1)(1 - \nu_{13} \epsilon_1)}{1 + \epsilon_1}. \quad (\text{B.1})$$

The effect of neglecting the geometrical changes g is presented here on a synthetic experiment. Assuming a harmonic stress $\sigma(t)$ acting on a specimen in the axial direction:

$$\sigma = \tilde{\sigma} \cos(2\pi f_{\text{exc}} t), \quad (\text{B.2})$$

causes, under the assumption of negligible viscoelastic behaviour, a harmonic resistivity change $d\rho(t)$ and a strain in the axial direction $\epsilon(t)$:

$$d\rho(t) = \pi \tilde{\sigma} \cos(2\pi f_{\text{exc}} t) = d\tilde{\rho}(t) \cos(2\pi f_{\text{exc}} t), \quad (\text{B.3})$$

$$\epsilon(t) = s \tilde{\sigma} \cos(2\pi f_{\text{exc}} t) = \tilde{\epsilon} \cos(2\pi f_{\text{exc}} t). \quad (\text{B.4})$$

By introducing the ratio r between the resistivity change amplitude $d\tilde{\rho}$ and the strain amplitude $\tilde{\varepsilon}$

$$r = \frac{d\tilde{\rho}}{\tilde{\varepsilon}}, \quad (\text{B.5})$$

and rearranging Eqs. (20), (23), (B.3), (B.4), resistivity not corrected for geometrical changes $h(t)$ is:

$$h(t) = R(t) \frac{l_2 l_3}{l_E} = \left[\rho_0 + r \tilde{\varepsilon} \cos(2\pi f_{\text{exc}} t) \right] \frac{1 + \tilde{\varepsilon} \cos(2\pi f_{\text{exc}} t)}{\left(1 - \nu \tilde{\varepsilon} \cos(2\pi f_{\text{exc}} t)\right)^2}, \quad (\text{B.6})$$

where the Poisson's ratios in different directions are assumed to be equal $\nu = \nu_{12} = \nu_{13}$. When the geometrical changes are neglected, $h(t)$ represents the time signal used for the identification of the initial resistivity $\rho_{0\text{I}}$ and the amplitude of resistivity change $d\tilde{\rho}_{\text{I}}$. Index I denotes the identified quantities. Transforming $h(t)$ into the frequency-domain $\tilde{h}(f)$ using a Fourier transform, the initial resistivity and the resistivity change are determined from Eqs. (24), (25) as:

$$\rho_{0\text{I}} = \tilde{h}(f = 0), \quad (\text{B.7})$$

$$d\tilde{\rho}_{0\text{I}} = \tilde{h}(f_{\text{exc}}). \quad (\text{B.8})$$

The synthetic function $h(t)$ was generated from the parameters $f_{\text{exc}} = 55$ Hz, $\rho_0 = 0.1 \Omega\text{m}$, $\tilde{\varepsilon} = 10^{-3}$, $\nu = 0.25$ and focusing the analysis on the interval $r \in (10^{-6}, 10^4) \Omega\text{m}$. In this synthetic experiment, for different ratios r , the amplitude of the resistivity change $d\tilde{\rho}_{\text{I}}$ was identified. In Fig. B.8 a) the identified increment $d\tilde{\rho}_{\text{I}}$ normalised by the true increment $d\tilde{\rho}$ is shown. For low ratios, the geometrical changes predominantly cause a change of the resistance. As a result, significantly higher resistivity increments are identified. When the ratio r increases, the resistivity change is the main cause of the resistance change. Additionally, the parameters ε , ν and ρ_0 were varied. A negligible influence of the strain variations was observed. A slight influence of the Poisson's ratio ν variations and a significant influence of the initial resistivity ρ_0 variation were observed, see Fig. B.8 c) and b), respectively. The synthetic experiment shows that the geometrical changes should not be neglected, since a significant influence on the identified resistivity was observed.

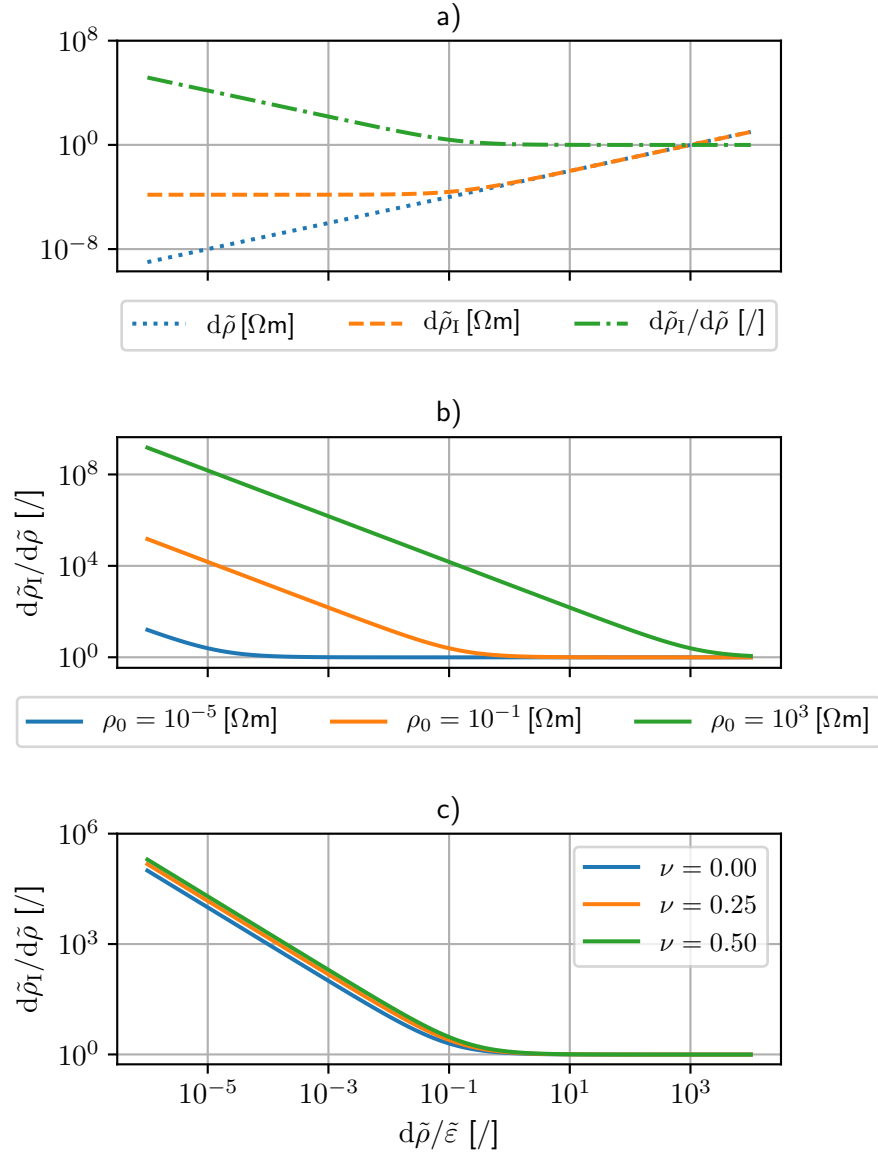


Figure B.8: The influence of ratio $r = d\tilde{\rho}/\tilde{\epsilon}$ on the ratio between identified increment of resistivity $d\tilde{\rho}_I$ and true increment of resistivity $d\tilde{\rho}$ when parameters a) $f_{\text{exc}} = 55$ Hz, $\rho_0 = 0.1$ Ωm, $\tilde{\epsilon} = 10^{-3}$, $\nu = 0.25$, b) $f_{\text{exc}} = 55$ Hz, $\tilde{\epsilon} = 10^{-3}$, $\nu = 0.25$, c) $f_{\text{exc}} = 55$ Hz, $\rho_0 = 0.1$ Ωm, $\tilde{\epsilon} = 10^{-3}$ are used

References

- [1] J. Oliveira, V. Correia, H. Castro, P. Martins, and S. Lanceros-Mendez. Polymer-based smart materials by printing technologies: Improving application and integration. *Additive Manufacturing*, 21:269 – 283, 2018.
- [2] F. García Ferré, A. Johansson, L. Herrmann, J. Korbel, T. Erford, and U. Riechert. A lightweight electromagnetic actuator for high voltage dc power grids. *Additive Manufacturing*, 27:533 – 539, 2019.
- [3] Cassidy Silbernagel, Ian Ashcroft, Phill Dickens, and Michael Galea. Electrical resistivity of additively manufactured als10mg for use in electric motors. *Additive Manufacturing*, 21:395 – 403, 2018.
- [4] Andrea Bellacicca, Tommaso Santaniello, and Paolo Milani. Embedding electronics in 3d printed structures by combining fused filament fabrication and supersonic cluster beam deposition. *Additive Manufacturing*, 24:60 – 66, 2018.
- [5] John M. Gardner, Godfrey Sauti, Jae-Woo Kim, Roberto J. Cano, Russell A. Wincheski, Christopher J. Stelter, Brian W. Grimsley, Dennis C. Working, and Emilie J. Siochi. 3-d printing of multifunctional carbon nanotube yarn reinforced components. *Additive Manufacturing*, 12:38 – 44, 2016.
- [6] Mohammad Shojib Hossain, Jose A. Gonzalez, Ricardo Martinez Hernandez, Mohammad Arif Ishtiaque Shuvo, Jorge Mireles, Ahsan Choudhuri, Yirong Lin, and Ryan B. Wicker. Fabrication of smart parts using powder bed fusion additive manufacturing technology. *Additive Manufacturing*, 10:58 – 66, 2016.
- [7] Md Omar Faruk Emon, Faez Alkadi, Daryl George Philip, Da-Hye Kim, Kyung-Chang Lee, and Jae-Won Choi. Multi-material 3d printing of a soft pressure sensor. *Additive Manufacturing*, 28:629 – 638, 2019.
- [8] Min-Hang Bao. Micro mechanical transducers: pressure sensors, accelerometers, and gyroscopes. In *Handbook of sensors and actuators*, volume 8, chapter 1, page 378. ELSEVIER B.V., 2000.
- [9] Simon J. Leigh, Robert J. Bradley, Christopher P. Pursell, Duncan R. Billson, and David A. Hutchins. A Simple, Low-Cost Conductive Composite Material for 3D Printing of Electronic Sensors. *PLoS ONE*, 7(11):1–6, 2012.

- [10] Meshari Alsharari, Baixin Chen, and Wenmiao Shu. 3D Printing of Highly Stretchable and Sensitive Strain Sensors Using Graphene Based Composites. *Proceedings*, 2(13):792, 2018.
- [11] Josef F. Christ, Nahal Aliheidari, Amir Ameli, and Petra Pötschke. 3D printed highly elastic strain sensors of multiwalled carbon nanotube/thermoplastic polyurethane nanocomposites. *Materials and Design*, 131:394–401, 2017.
- [12] Jesse Gooding, James F. Mahoney, and Travis Fields. 3D Printed Strain Gauge Geometry and Orientation for Embedded Sensing. In *58th AIAA/ASCE/AHS/ASC Structures, Structural Dynamics, and Materials Conference*, number January, pages 1–14. American Institute of Aeronautics and Astronautics Inc, AIAA, 2017.
- [13] Kyuyoung Kim, Jaeho Park, Ji hoon Suh, Minseong Kim, Yongrok Jeong, and Inkyu Park. 3D printing of multiaxial force sensors using carbon nanotube (CNT)/thermoplastic polyurethane (TPU) filaments. *Sensors and Actuators, A: Physical*, 263:493–500, 2017.
- [14] Mohammed Al-Rubai, Ryohei Tsuruta, Umesh Gandhi, Chuan Wang, and Xiaobo Tan. A 3D-printed stretchable strain sensor for wind sensing. *Smart Materials and Structures*, 28(8):084001, 2019.
- [15] Marco Maurizi, Janko Slavič, Filippo Cianetti, Marko Jerman, Joško Valentinčič, Andrej Lebar, and Miha Boltežar. Dynamic measurements using FDM 3D-printed embedded strain sensors. *Sensors (Switzerland)*, 19(12):1–15, 2019.
- [16] A. S. Fiorillo, C. D. Critello, and A. S. Pullano. Theory, technology and applications of piezoresistive sensors: A review. *Sensors and Actuators, A: Physical*, 281:156–175, 2018.
- [17] Jan Chan Huang. Carbon black filled conducting polymers and polymer blends. *Advances in Polymer Technology*, 21(4):299–313, 2002.
- [18] Sithiprumnea Dul, Luca Famrbi, and Alessandro Pegoretti. Filaments Production and Fused Deposition Modelling of ABS/Carbon Nanotubes Composites. *Nanomaterials*, 8(1):49, 2018.
- [19] A. Dorigato, V. Moretti, S. Dul, S. H. Unterberger, and A. Pegoretti. Electrically conductive nanocomposites for fused deposition modelling. *Synthetic Metals*, 226:7–14, 2017.

- [20] J. C. Tan and H. Y. Low. Embedded electrical tracks in 3D printed objects by fused filament fabrication of highly conductive composites. *Additive Manufacturing*, 23(June):294–302, 2018.
- [21] Sen Wai Kwok, Kok Hin Henry Goh, Zer Dong Tan, Siew Ting Melissa Tan, Weng Weei Tjiu, Je Yeong Soh, Zheng Jie Glenn Ng, Yan Zhi Chan, Hui Kim Hui, and Kuan Eng Johnson Goh. Electrically conductive filament for 3D-printed circuits and sensors. *Applied Materials Today*, 9:167–175, 2017.
- [22] Benedikt Hampel, Samuel Monshausen, and Meinhard Schilling. Properties and applications of electrically conductive thermoplastics for additive manufacturing of sensors. *Technisches Messen*, 84(9):593–599, 2017.
- [23] Jie Zhang, Bin Yang, Feng Fu, Fusheng You, Xiuzhen Dong, and Meng Dai. Resistivity and Its Anisotropy Characterization of 3D-Printed Acrylonitrile Butadiene Styrene Copolymer (ABS)/Carbon Black (CB) Composites. *Applied Sciences*, 7(1):20, 2017.
- [24] Hagen Watschke, Karl Hilbig, and Thomas Vietor. Design and Characterization of Electrically Conductive Structures Additively Manufactured by Material Extrusion. *Applied Sciences*, 9(4):779, 2019.
- [25] Patrick F. Flowers, Christopher Reyes, Shengrong Ye, Myung Jun Kim, and Benjamin J. Wiley. 3d printing electronic components and circuits with conductive thermoplastic filament. *Additive Manufacturing*, 18:156 – 163, 2017.
- [26] Yingjun Zhao, Sandra Gschossmann, Martin Schagerl, Patrick Gruener, and Christoph Kralovec. Characterization of the spatial elastoresistivity of inkjet-printed carbon nanotube thin films. *Smart Materials and Structures*, 27(10), 2018.
- [27] G. M. Koo and T. N. Tallman. Higher-order resistivity-strain relations for self-sensing nanocomposites subject to general deformations. *Composites Part B: Engineering*, 190(December 2019):107907, 2020.
- [28] Michael Dawoud, Iman Taha, and Samy J. Ebeid. Strain sensing behaviour of 3D printed carbon black filled ABS. *Journal of Manufacturing Processes*, 35(August):337–342, 2018.

- [29] Enrique Cuan-Urquizo, Eduardo Barocio, Viridiana Tejada-Ortigoza, R. Pipes, Ciro Rodriguez, and Armando Roman-Flores. Characterization of the mechanical properties of FFF structures and materials: A review on the experimental, computational and theoretical approaches. *Materials*, 12(6):895, March 2019.
- [30] Miquel Domingo-Espin, Josep M. Puigoriol-Forcada, Andres Amador Garcia-Granada, Jordi Llumà, Salvador Borros, and Guillermo Reyes. Mechanical property characterization and simulation of fused deposition modeling Polycarbonate parts. *Materials and Design*, 83:670–677, 2015.
- [31] Charles S. Smith. Macroscopic Symmetry and Properties of Crystals. *Solid State Physics - Advances in Research and Applications*, 6(C):175–249, 1958.
- [32] P. W. Bridgman. The effect of homogeneous mechanical stress on the electrical resistance of crystals. *Physical Review*, 42(6):858–863, 1932.
- [33] Charles S. Smith. Piezoresistance effect in germanium and silicon. *Physical Review*, 94(1):42–49, April 1954.
- [34] J. N. Reddy. *An Introduction to Continuum Mechanics*. Cambridge University Press, jul 2013.
- [35] Y. Song, Y. Li, W. Song, K. Yee, K.-Y. Lee, and V.L. Tagarielli. Measurements of the mechanical response of unidirectional 3d-printed PLA. *Materials & Design*, 123:154–164, June 2017.
- [36] Madhukar Somireddy and Aleksanderand Czekanski. Mechanical characterization of additively manufactured parts by FE modeling of mesostructure. *Journal of Manufacturing and Materials Processing*, 1(2):18, November 2017.
- [37] Technical data sheet - electrolube scp. https://electrolube.com/knowledge_base/scp-technical-data-sheet/. Last accessed 6. March 2020.
- [38] Technical data sheet - embossed tin-plated copper foil tape 1345 3m. <https://multimedia.3m.com/mws/media/373860/3m-embossed-tin-plated-copper-foil-tape-1345.pdf>. Last accessed 6. March 2020.

- [39] John G. Webster, editor. *Electrical Measurement, Signal Processing, and Displays (Principles and Applications in Engineering)*. CRC Press, jul 2003.
- [40] Edward M. Purcell. *Electricity and Magnetism*. Cambridge University Press, jan 2013.
- [41] Technical data - proto-pasta conductive pla. <https://www.proto-pasta.com/products/conductive-pla>. Last accessed 6 March 2020.
- [42] Nuwan Munasinghe, Matthew Woods, Lewis Miles, and Gavin Paul. 3-D Printed Strain Sensor for Structural Health Monitoring. *International Conference on Cybernetics and Intelligent Systems (CIS) and International Conference on Robotics, Automation and Mechatronics (RAM)*, (November), 2019.
- [43] Pauli Virtanen, , Ralf Gommers, Travis E. Oliphant, Matt Haberland, Tyler Reddy, David Cournapeau, Evgeni Burovski, Pearu Peterson, Warren Weckesser, Jonathan Bright, Stéfan J. van der Walt, Matthew Brett, Joshua Wilson, K. Jarrod Millman, Nikolay Mayorov, Andrew R. J. Nelson, Eric Jones, Robert Kern, Eric Larson, C J Carey, İlhan Polat, Yu Feng, Eric W. Moore, Jake VanderPlas, Denis Laxalde, Josef Perktold, Robert Cimrman, Ian Henriksen, E. A. Quintero, Charles R. Harris, Anne M. Archibald, Antônio H. Ribeiro, Fabian Pedregosa, and Paul van Mulbregt. SciPy 1.0: fundamental algorithms for scientific computing in python. *Nature Methods*, 17(3):261–272, February 2020.
- [44] J. M. Chacón, M. A. Caminero, E. García-Plaza, and P. J. Núñez. Additive manufacturing of PLA structures using fused deposition modelling: Effect of process parameters on mechanical properties and their optimal selection. *Materials and Design*, 124:143–157, 2017.
- [45] Tianyun Yao, Juan Ye, Zichen Deng, Kai Zhang, Yongbin Ma, and Huangjiang Ouyang. Tensile failure strength and separation angle of FDM 3D printing PLA material: Experimental and theoretical analyses. *Composites Part B: Engineering*, 188(January):107894, 2020.